Check for
updates

Effects of Localized Micro-blowing on a Spatially Developing Flat Turbulent Boundary Layer

Lan Xie[1] · Yao Zheng[1] · Yang Zhang[1] · Zhi-xian Ye[1] · Jian-feng Zou[1]

Abstract

Direct numerical simulation (DNS) is used to investigate the turbulent flat-plate boundary layer with localized micro-blowing. The 32×32 array of micro-holes is arranged in a staggered pattern on the solid wall, located in the developed turbulent region. The porosity of the porous wall is 23%, and the blowing fraction is 0.0015. The Reynolds number based on the inflow velocity is set to be 50,000. The structures of the turbulent boundary layer are carefully analyzed to understand the effects of micro-blowing and its drag reduction mechanism. The DNS results show that the drag reduction is efficient, and the local maximum rate of drag reduction achieves 40%. A low-speed "turbulent spot" near the micro-blowing region thickens the boundary layer. Some turbulent properties, such as the mean velocity profile, stream-wise vorticity and stream-wise velocity fluctuation are lifted up. Particularly, the tilting term of vorticity transport is significantly increased. Meanwhile, the visualization of 3-dimensional vortex displays several concave marks on the surface of the near-wall vortices, which is caused by the micro-jets, leading to more broken vortices and isotropic small scales. This impact travels downstream with a small distance due to the accumulation of the micro-jets, while the uplift effect will gradually disappear. In addition, FIK identity reveals that the spatial development term and mean wall-normal convection term play opposite roles in the contribution to the skin friction drag.

Keywords Drag reduction · Turbulent boundary layer · Micro-blowing · Vorticity

1 Introduction

The techniques of drag reduction via the flow control have caught huge attention of the aviation industry. To a civil or commercial aircraft, about 40–50% of the whole drag during cruising comes from the skin friction in the turbulent boundary layer. It is believed that 1% drag reduction of an aircraft such as A340 can possibly save about 400,000 L of fuel per year (Kornilov and Boiko 2014; Kornilov 2015). Many ideas of skin-friction drag reduction have been proposed, such as riblets (Choi et al. 1993), permeable coatings

✉ Yang Zhang
yangzhang@zju.edu.cn

[1] Center for Engineering and Scientific Computation, and School of Aeronautics and Astronautics, Zhejiang University, Hangzhou 310027, China

(Abderrahaman-Elena and García-Mayoral 2017), span-wise wall oscillation (Lardeau and Leschziner 2013), and travelling wave control (Du and Karniadakis 2000). As an effective drag reduction strategy, blowing control, which has already been stimulated, exerted on the wall surface with vertical injection air, has shown a wide range of research (Sumitani and Kasagi 1995; Park and Choi 1999; Krogstad and Kourakine 2000; Chung and Sung 2001; Chung et al. 2002; Keirsbulck et al. 2006; Kim and Sung 2006; Araya et al. 2011; Kametani et al. 2015; Kametani and Fukagata 2011; Hwang 1997) and application value. A variety of blowing methods have been investigated, including uniform blowing or suction, periodic blowing, micro-blowing, blowing/suction feedback and so on. Blowing from the wall can decrease the skin friction by thickening the turbulent boundary layer, but will increase the strength of the fluctuating quantities (Sumitani and Kasagi 1995).

Park and Choi (1999) performed DNS to investigate the effects of uniform blowing or suction from a span-wise slot in a fully developed turbulent channel flow. The intensity of blowing or suction was less than 10% of the free-stream velocity. In the case of uniform blowing, an upward shift in the log layer is observed, and the stream-wise vortices are lifted up, thus the interaction between the near-wall vortices and the wall becomes weaker. However, the result of uniform suction is opposite. These findings are also demonstrated experimentally by Krogstad and Kourakine (2000) with blowing localized in a porous strip. A smaller intensity of injection (less than 1% of free-stream velocity) under zero pressure gradient condition was adopted to prevent flow separation. They found that the injection increases all the Reynolds stresses, and this effect will not disappear immediately, but extends downstream with a distance. The affected layer is sandwiched between the outer edge of the incoming boundary layer and a new layer that quickly develops on the wall. Although there is no effect of the blowing rate on the flow anisotropy, the shear stresses from different quadrants are affected. Interestingly, the DNS computation of Chung et al. (Chung and Sung 2001; Chung et al. 2002) revealed that blowing decreases the anisotropy of the near-wall turbulent structure by an anisotropic invariant map. Meanwhile, the relaxation of the anisotropy turbulence associated with blowing is much quicker than that with suction. It is further verified by the experiments of Keirsbulck et al. (2006). In addition, several studies (Kim and Sung 2006; Araya et al. 2011) about the effects of unsteady time-periodic blowing showed some differences in Reynolds shear stress, stream-wise vorticity fluctuations and energy redistribution. Kametani and Fukagata (Kametani et al. 2015; Kametani and Fukagata 2011) focused on the skin friction reduction on the spatially developing turbulent boundary layers with uniform blowing (UB) or suction in many of their studies. The amplitude of the blowing/suction control is very small with 0.1% of the free-stream velocity, but more than 10% of drag reduction rate is achieved by means of blowing, and the maximum net-energy-saving rate is over 20% at the end of the blowing region. They suggested that a longer stream-wise length of uniform blowing is necessary in order to obtain a larger drag reduction and energy efficiency. By dynamical decomposition of the skin friction, the mean convection term is found to be a big positive contribution to the drag reduction in the UB case. It overwhelms the negative turbulent contribution which is enhanced away from the wall, so the overall drag reduction effect is achieved by UB.

In current study, we address the micro-blowing technique (MBT) in the application of drag reduction on the turbulent boundary layer, which was firstly proposed by Hwang (1997) of NASA Glenn Research Center (GRC). In this method, an extremely small amount of air is blown vertically through several tiny holes to modify the velocity profile of the turbulent boundary layer, which will lead to the reduction of skin friction. The similarity to the previous uniform blowing in Kametani et al. (2016) is the very weak blowing amplitude, but their blowing methods are different. Although the

intermittent blowing effect at moderate Reynolds numbers has also been investigated, the blowing in each section still keeps continuous and uniform. In MBT, generally, the discrete arrangement of micro-holes with the diameter being 0.1–0.4 mm (e.g. PN2 or PN3 porous plates with small roughness) is the most obvious characteristics, as well as the low injection intensity with blowing fraction below 0.01. Many experiments and simulations (Hwang 2004) proved that over 50% reduction of skin friction has been achieved in a wide range of subsonic and supersonic flows. Following the pioneering work of Hwang (1997), experimental studies were investigated by Kornilov (2015) to prove the efficiency of micro-blowing through a permeable wall with several micro-holes. It is successfully obtained that the maximum reduction rate of local skin friction is 70%, and the total drag reduction is about 4.5–5%, while the blowing fraction ranged from 0 to 0.00287, which demonstrates the effectiveness by using relatively low amount of blowing air (Kornilov and Boiko 2012). Also, similar blowing mechanism for the skin-friction reduction was reported, such as an upshift of the near-wall boundary-layer region from the wall and the thickening of the viscous sub-layer.

Despite this, there are still only few studies about the micro-blowing technique in the turbulent drag reduction. Moreover, the past studies about micro-blowing mainly focused on the quantification of the drag-reduction level and its dependence on the control parameters such as the configuration of micro-holes or the blowing strength (Kornilov and Boiko 2014; Hwang 2004). Although Kametani et al. (2015) have revealed the effect of turbulent scales by weak uniform blowing in the inner-region and outer region and the weak injections enhance the small and short wavelength component near the wall, the underlying turbulence mechanisms of the interaction between the micro-injections and turbulent boundary layer still cannot be fully understood. Based on this, we focus on the analysis of turbulence information changes in a spatially evolving flat-plate turbulent boundary layer, and then make a detailed comparison between the basic flow and the modified flow with micro-blowing.

It is worthy remarking that this paper emphasizes the evolution of drag reduction in the developing turbulent boundary layer on a flat plate, which is closer to the practical situation of the aircraft surface, rather than in an internal turbulent channel. Furthermore, the drag contributions are totally different between the fully developed turbulent flow and the spatially developing turbulence flow, although the control scheme yields the similar drag reduction rate. A comparison study in the opposite control of blowing/suction by Stroh et al. (2015) indicated that the achievable drag reduction in turbulent channel flow is mostly based on the attenuation of the Reynolds shear stress, while the spatial flow development is dominated by the spatially evolving turbulent boundary layer. The fact that the mean convection term-UV in the turbulent flat-plate boundary layer plays a decisive role in drag reduction, which is also confirmed in the study of Kametani and Fukagata (Kametani et al. 2015; Kametani and Fukagata 2011) with uniform blowing.

In this paper, a spatially developing flat-plate boundary layer with localized micro-blowing at free-stream Mach number 0.7 is resolved by DNS. The differences in flow filed with and without blowing are compared by the mean properties and the fluctuation information. The purpose is to explore the change of turbulence structures caused by localized micro-blowing. The mechanism of drag reduction is also discussed by using the FIK identity (Fukagata et al. 2002). The rest of the paper is organized as follows: numerical details including computational setup of the basic case and the modified case are given in Sect. 2, with a short note on validation. Then detailed analyses of the modified turbulent boundary layer are presented in Sect. 3. Finally, a summary is provided in Sect. 4.

2 Numerical Details

2.1 Numerical Method and Setup

We perform a DNS of spatial developing flat-plate turbulent boundary layer by solving three-dimensional (3D) compressible Navies-Stokes equations. A seventh-order accurate upwind finite difference scheme is adopted for the discretization of convection terms, and the diffusion terms are approximated by an eight-order accurate central difference scheme. For temporal advancement, a three-order TVD type Runge–Kutta method is used. The details of the DNS solver can be found in De-xun et al. (Fu Et Al. 2010; Ying et al. 2007). Notably, the flow variables, density ρ, stream-wise velocity u, normal velocity v, span-wise velocity w, temperature T and pressure p in the DNS code are non-dimensioned by the corresponding free-stream parameters ρ_∞, U_∞, T_∞, $\rho_\infty U_\infty^2$, respectively (the symbol ∞ means the free stream). In the current simulation, if not specified, the length is non-dimensioned by using inch (in).

The entire computational domain is bounded by inlet and outlet boundaries, an upper boundary, a wall boundary, and two span-wise boundaries, as shown in Fig. 1. The coordinate x, y, and z correspond to the stream-wise, wall-normal, and span-wise directions, respectively. No-slip and isothermal conditions are imposed to the solid wall. The upper and outlet boundaries are set as non-reflective condition to allow acoustic perturbation to spread out (Poinsot and Lelef 1992), and the periodic condition is applied in the span-wise boundary.

The Mach number Ma_∞ of the free stream is 0.7, and the Reynolds number Re_∞ is 50,000 by using one characteristic length $L_\infty = 1$ inch. In order to give the inlet boundary condition and the initial flow of the entire 3D computational domain, a DNS of two-dimensional (2D) flat-plate flow with the same free stream has been performed in advance to obtain a laminar compressible similarity solution. The coordinates of 2D domain in x and y directions are $0 \le x \le 35$ and $0 \le y \le 0.65$. When the 2D calculation has developed into a stationary state, the available laminar boundary layer solution at the section of $x=30$ is stored as the inlet condition and the flow initialization for 3D computation. The initial Reynolds number $Re_{\delta_d^0}$ at $x=30$ is 500 based on the inflow displacement thickness δ_d^0. The 3D computational box is $30 \le x \le 42$, $0 \le y \le 0.65$ and $0 \le z \le 1.57$ which corresponds to $L_x \times L_y \times L_z = 1200\delta_d^0 \times 65\delta_d^0 \times 157\delta_d^0$. Its width and height are selected to be at least twice the largest 99% boundary thickness δ_{99}. The analyses of the two-point correlations have
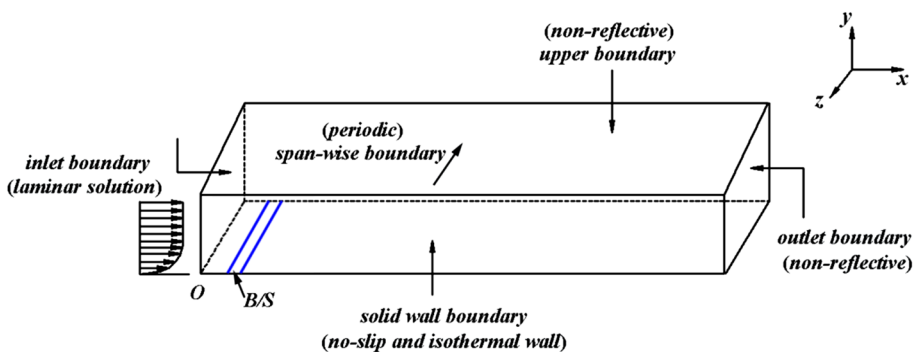

Fig. 1 Sketch of the computational flat plate

confirmed that it is enough wide to avoid affecting turbulence dynamic in the span-wise direction. The grids are uniform in both x and z directions with $N_x = 1000$ and $N_z = 320$ being the number of points, and they are stretched in the wall normal direction by an exponential function. The grid resolution in viscous units is $\Delta x^+ = 20.26$, $\Delta y_w^+ = 1.01$ and $\Delta z^+ = 10.13$. The stream-wise resolution is approximately equal to the drag reduction study with uniform blowing in the developing turbulent boundary layers by Kametani et al. (2015), but is slightly less than the comparative study of DNS and experiments of turbulent boundary layers up to $Re_\theta = 2500$ where θ is the boundary layer momentum–loss thickness (Schlatter et al. 2009). The specific parameters in the present computations are listed in Table 1.

In order to accelerate the laminar-to-turbulent transition, a local blowing/suction (B/S) control on the wall is applied to the region that is close to the inlet, shown in Fig. 1, where the wall-normal velocity component is prescribed by,

$$v(x, z, t) = AU_\infty f(x)g(z)h(t), \ x_a \leq x \leq x_b \tag{2-1}$$

with $A = 0.12$, which is the amplitude of the disturbance, and its value is more than that chosen by Pirozzoli et al. (2004), in order to accelerate the turbulence transition. The stream-wise, span-wise and time-dependent control functions are defined as follows,

$$f(x) = 4 \sin\left[2\pi\left(x - x_a\right)\middle/\left(x_b - x_a\right)\right](1 - \cos\theta)\middle/\sqrt{27},$$

$$g(z) = \sum_{l=1}^{l_{max}} Z_l \sin\left[2\pi l\left(z/L_z + \phi_l\right)\right],$$

$$\sum_{l=1}^{l_{max}} Z_l = 1, \ Z_l = 1.25Z_{l+1}, \tag{2-2}$$

Table 1 Computational parameters

| Quantity	Symbol	Value
Domain coordinates (x, y, z)	2D	([0, 35], [0, 0.65], 0) (inch)
	3D	([30, 42], [0, 0.65], [0, 1.57]) (inch)
Numbers of grid points	$N_x \times N_y \times N_z$	$1000 \times 100 \times 320$
Spatial resolution	$\Delta x^+ \times \Delta y_w^+ \times \Delta z^+$	$20.26 \times 1.01 \times 10.13$
Wall temperature	T_w/T_∞	1.098
Characteristic length	L_∞	1 (inch)
Free stream	ρ_∞	0.1484 (kg/m^3)
	U_∞	237.7 (m/s)
	T_∞	288 (K)
	Ma_∞	0.7
	Re_∞	50,000
Initial displacement Reynolds number	$Re_{\delta_d^0}$	500

$$h(t) = \sum_{m=1}^{m_{max}} T_m \sin\left(\beta t + 2\pi\phi_m\right),$$

$$\sum_{m=1}^{m_{max}} T_m = 1, \; T_m = 1.25 T_{m+1}.$$

The coordinates x_a and x_b are the start and end of the B/S region, L_z is the span-wise length of the domain, the disturbance frequency β is 75000 Hz which is adopted by Pirozzoli et al. (2004), and the random numbers ϕ_l and ϕ_m ranges from 0 to 1.

2.2 Basic Flow and Validation

Based on the numerical model definition above, a basic turbulent flow has been solved before the discussion about the effects of micro-blowing on the turbulent boundary layer. The spatial development of the boundary layer is presented in Fig. 2. The boundary-layer thickness δ_{99}/L_∞, the momentum Reynolds number Re_θ, and the displacement Reynolds number $Re_{\delta d}$ are all growing in the stream-wise direction, as shown in Fig. 2a. These symbols and lines represent the sampling data points and corresponding fitting curves. The initial momentum–loss Reynolds number at the entrance is about 192 and gradually rises up to 1500 in the downstream. The shape factor H_{12}, the ratio of δ_d and θ, is depicted in Fig. 2b and is a good indicator of the mean stream-wise velocity profile in the boundary layer. At present study, the starting value, $H_{12} \approx 2.3$, firstly experiments a rapid decline and then reaches a smooth trend beyond $Re_\theta \approx 1000$. The literature lines from Schlatter et al. (2009) and Schlatter and Örlü (2010, 2012) show some differences during the descent due to the tripping effects but tend to the almost coincident line eventually. It indicates that the state of the boundary layer at $Re_\theta \geq 700$ has a satisfactory agreement with the DNS of Schlatter and Örlü (2010, 2012) when turbulence is sufficiently developed downstream.
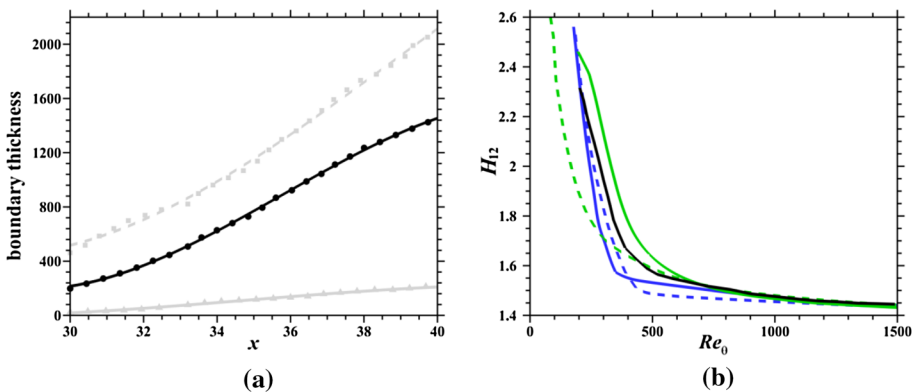

Fig. 2 Spatial development of the boundary layer. **a** boundary-layer thickness: solid black line, Re_θ; dashed grey line, $Re_{\delta d}$; solid grey line, $1000\delta_{99}/L_\infty$. **b** Shape factor H_{12}: solid blue line, Schlatter et al. (2009); dashed blue line, Schlatter and Örlü (2010); two green lines, TS and LA tripping in Schlatter and Örlü (2012); solid black line: present DNS

Fig. 3 Friction velocity U_τ as a function of Re_θ (symbol square: Wu and Moin (2010); symbol circle: Komminaho and Skote (2002); symbol diamond: $2\left(U_\tau/U_\infty\right)^2 = c_f = 0.024 Re_\theta^{-0.25}$; solid line: present DNS)
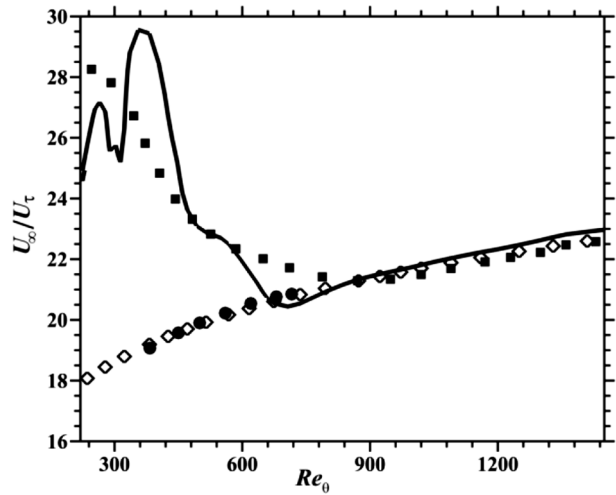
Fig. 4 Root mean square (RMS) of velocity fluctuations
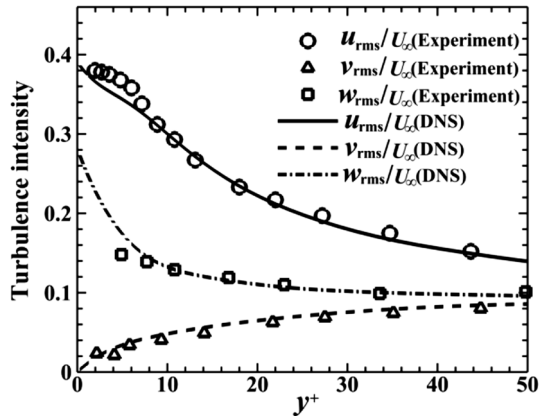
The characteristic mean velocity U_∞/U_τ of the boundary layer is depicted in Fig. 3 as a function of Re_θ. The friction velocity U_τ is obtained by $U_\tau = \sqrt{\tau_w/\rho}$ as the relevant velocity scale through the boundary layer. The skin-friction coefficient c_f can be also derived from the friction velocity scaled by the free stream velocity. Surprisingly, our calculation results are well consistent with the simple empirical correlation $c_f = 0.024 Re_\theta^{-0.25}$, Smits et al. 1983) in the downstream of turbulent boundary layer $Re_\theta > 680$. In addition, the scattered points from the calculation data of Wu and Moin (2010) and Komminaho and Skote (2002) are also in reasonable agreement with the current DNS results and the relative deviation is below 3%.

The distribution of turbulent intensity along the normal wall direction at $x = 39.9$ is shown in Fig. 4 where $u_{rms} = \sqrt{u'^2}, v_{rms} = \sqrt{v'^2}, w_{rms} = \sqrt{w'^2}$ (the superscript ' indicates the fluctuation). In the near wall region, the fluctuation of steam-wise velocity component is the strongest and the normal component is the weakest. This shows the anisotropy of turbulent flow. With the distance away from the wall, the RMS values of all velocity components gradually decrease and appear to be uniform, which indicates that the turbulent fluctuation in the outer boundary layer is weak and tends to be isotropic. Current calculation

results reach an agreement with the experimental data (Karlsson and Johansson 1986), which demonstrates that the present numerical methods and setup can accurately predict the turbulent fluctuation information.

2.3 Micro-Blowing Modified Flow

Based on the analyses of the basic flow above, in order to investigate the effects of MBT on the turbulent boundary layer, the chosen area of localized micro-blowing is located at $x> = 36$, where the flow has already transitioned to spatial developing turbulence. The NASA-PN2 porous plate (Hwang 2004) is adopted, and the diameter D is 0.0065. The holes are arranged in a staggered pattern on the x–y section of the solid wall, and a 32×32 array of the holes is numbered from left to right in sequence, as shown in Fig. 5. The spacing between centers of adjacent holes is $h_s = 0.0085$, which ensures the porosity of 23%.

It is reported that the large mass jet-flow with a vertical injection (perpendicular to the inflow) may cause flow separation and a large penalty of skin friction, which is not the result we expect in consideration of energy efficiency. The design of small mass flux and micro-holes is the special feature and advantage of MBT, because of the less energy injection and the large drag reduction of skin friction. The blowing fraction F is 0.0015 with $F = \rho_J V_J / \rho_\infty U_\infty$, where the subscript J represents the micro-blowing jet. Air is chosen to be the gas medium of micro-jet as the same as inflow. The temperature is $T_J = 0.868$, which is cooler than the free stream. This gives a density ratio DR of 1.2 (DR: micro-jet/free inflow). The geometry of micro-blowing channel is not considered in the present study, so the blowing input boundary condition can be regarded as uniform velocity and temperature
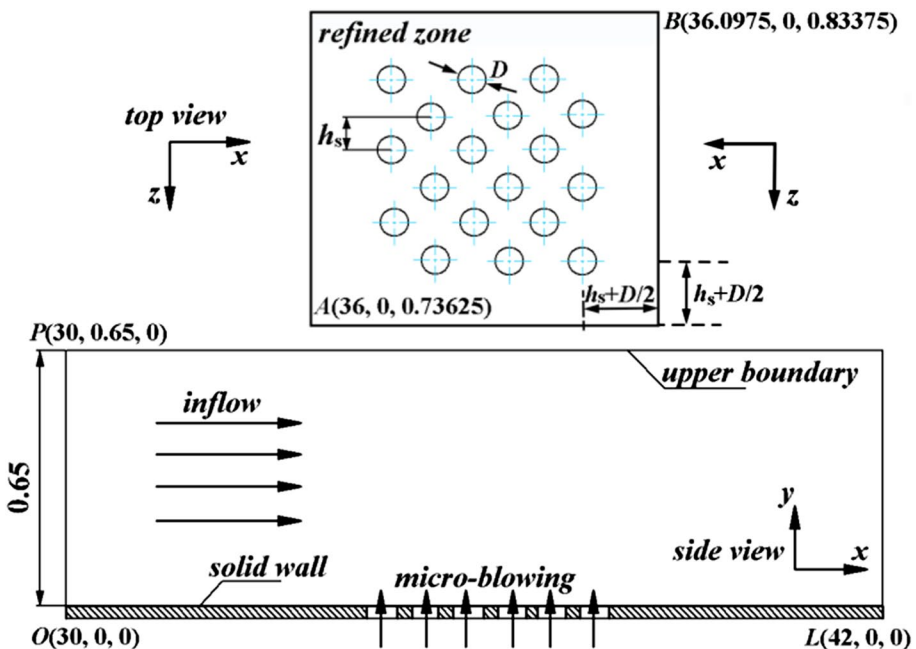

Fig. 5 Sketch of Micro-blowing from different perspectives

at the micro-hole wall. As for the micro-blowing region, a further refined mesh distribution is necessary to simulate the relatively smaller turbulent structures. There are 8 nodes set on one diameter of each micro-hole, so the grid spacing is $0.068\Delta x$(Δx is the grid size in the basic flow), see Fig. 6. Additionally, the refinement area is expanded outward with a distance of $h_s+D/2$ to obtain a more detailed description near the micro-holes, see the top view in Fig. 6. Thus, the total number of nodes is up to be $1232\times100\times416$. The detail parameters are listed in Table 2.

3 Simulation Results and Discusses

3.1 Skin-Friction Drag

The development of the local skin-friction coefficient,$c_f = \tau_w/(\rho_\infty U_\infty^2/2)$, along the stream-wise x-direction is plotted in Fig. 7, where τ_w and U_∞ denote the wall-shear stress and the inflow velocity, respectively. The vertical micro-blowing through the solid wall
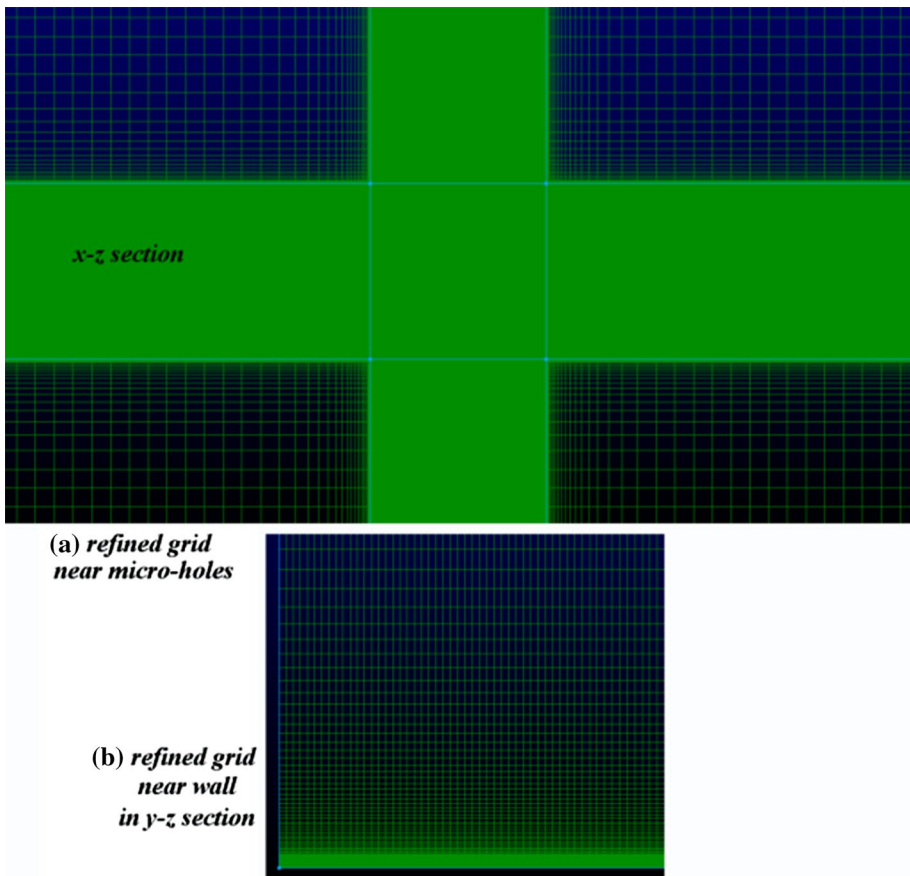

Fig. 6 Schematic diagrams of grid distributions in different sections

Table 2 Computational parameters in the micro-blowing case

Quantity	Symbol	Value
Hole diameter	D	0.0065
Hole spacing	h_s	0.0085
Porosity	ϕ	23%
Hole array	–	32×32
Numbers of grid points	$N_x \times N_y \times N_z$	$1232 \times 100 \times 416$
Refined grid spacing	$0.068\Delta x$	0.000816
Blowing fraction	F	0.0015
Injectant temperature	T_J	0.868
Density ratio	DR	1.2

Fig. 7 Mean skin friction drag (dashed: basic flow; filled dot: sampling point at the micro-blowing case; solid line: fitting curve at the micro-blowing case)
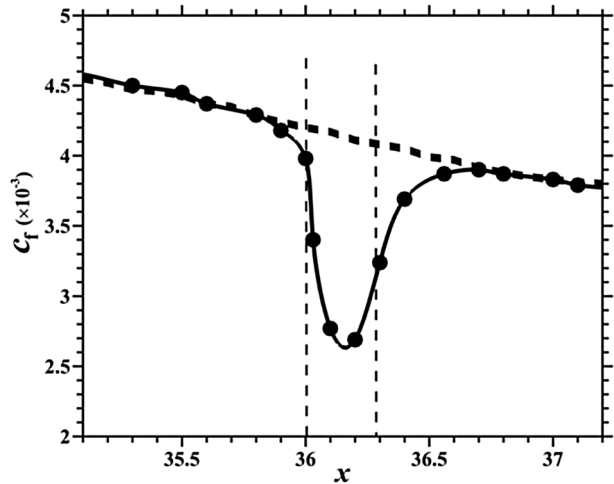
substantially reduces the skin friction coefficient c_f and the maximum reduction is up to 40%. Meanwhile, the area of the reduced c_f not only covers the entire micro-blowing region but also extends to a short distance in downstream. This is because the properties of boundary layer are impossible to recover to be the basic situation immediately even if it is out of the micro-blowing control. Hence, the viscous sub-layer has a memory of its previous state (Kornilov and Boiko 2014; Kornilov 2015).

In the case of achieving a drag reduction effect, it is important to assess the active control efficiency from the perspective of practical application. The local drag reduction rate, R^L, and the net-energy-saving rate, S^L, can be defined as

$$R^L(x) = \frac{c_{f0}(x) - c_f(x)}{c_{f0}(x)}, \tag{3-1}$$

$$S^L(x) = \frac{c_{f0}(x) - \left(c_f(x) + W_{in}(x)\right)}{c_{f0}(x)}, \tag{3-2}$$

where c_{f0} denotes the skin-friction drag in the basic flow without control. Hereby, W_{in} is the control-input power defined as
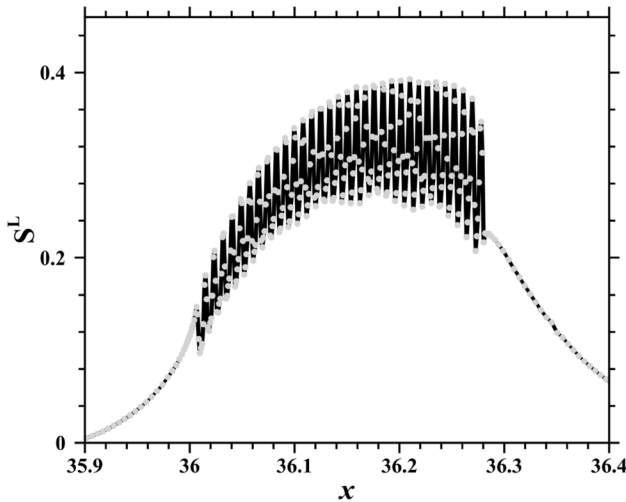
Fig. 8 Local net-energy saving rate (the solid grey dot represents the sampling point)

Table 3 The mean net-energy-saving rate and maximum drag reduction rate

References	Method of blowing	R^L (max) [%]	S (%)
Kornilov and Boiko (2014)	0.182–0.228% micro-blowing	71	15–25
Kametani et al. (2015)	0.1% uniform blowing	22	18
Kametani et al. (2016)	0.16–0.19% intermittent blowing	25–32	16.2–17.7
Tillman and Hwang (1999)	0.2% micro-blowing	50–70	–
Present	0.125% micro-blowing	40	23

$$W_{\text{in}}(x) = \Delta P_{\text{w}} V_{\text{w}}(x) + \frac{1}{2} V_{\text{w}}(x)^3, \tag{3-3}$$

where ΔP_{w} denotes the pressure difference between outside and inside of the blowing wall. It is noticed that the input energy of the micro-blowing control is very small due to the blowing amplitude, i.e.$V_{\text{w}} = 0.00125$, thus the drag reduction rate is almost equivalent to the net-energy-saving rate. Figure 8 descripts the local net-energy-saving rate as a function of the stream-wise location. Due to the staggered array of micro-blowing holes, the curve oscillates back and forth in the control area, but generally shows an increase in the down-stream distance. The mean net-energy-saving rate S can be defined as

$$S = \frac{1}{x_2 - x_1} \int_{x_1}^{x_2} S^L(x) dx, \tag{3-4}$$

where x_1 and x_2 denote the stream-wise locations where micro-blowing control starts and ends, respectively. In Table 3, approximately 23% mean net-energy-saving rate is achieved by micro-blowing with 0.125%U_∞ in present study. It is larger than the 0.1% uniform blowing or intermittent blowing in Kametani et al. (2016) due to a greater local drag reduc-tion rate in the micro-blowing technique. In the experiments with micro-blowing, 50–70%

reduction of skin friction drag is confirmed to be possible on the portions of the nacelle in Tillman and Hwang (1999). Kornilov and Boiko (2014) tested the permeable flat-plate and acquired the similar mean net-energy-saving rate of 15–25%.

3.2 Instantaneous Structures and Mean Properties

After applying micro-blowing control, we mainly compare the differences of turbulent structures and the changes of flow properties. The contours of instantaneous stream-wise velocity at three different x–z sections are shown in Fig. 9. The dotted line frame represents the micro-blowing control area. In the near-wall region at $y^+ = 6.8$, a lower speed "turbulent spot" in the blowing-control region is clearly observed in relation to the surroundings. This spot will leads to an area of lower velocity gradient close to the wall, and causes a change of wall skin friction. That's why the micro-blowing technique is widely used to reduce drag in engineering. Moreover, the turbulent spot area exceeds the control region and extends downstream, which proves the late effect of micro-blowing in the downstream. As the velocity increases absolutely away from the wall, the area of the low speed turbulent spot decreases (such as $y^+ = 14.7$), but the impact in the downstream is still evident. At $y^+ = 32.9$, the spot is not that obvious anymore.

Figure 10 visualizes the streamlines and stream-wise velocity distributions in the near-wall region close to the micro-holes in the span-wise section at $z = L_z/2$. Capital U and V stand for the time-averaged velocity components. The vertical jet from the micro-holes deflects downstream with the influence of upstream inflow. Gradually, the inflow streamline is slightly upward inclined in turn, and a few uneven and curved contour lines of U can be clearly seen in 10a and 10b. This is obviously the result of jet impingement. Compared with the basic flow, the thickness of viscous sub-layer increases strikingly,
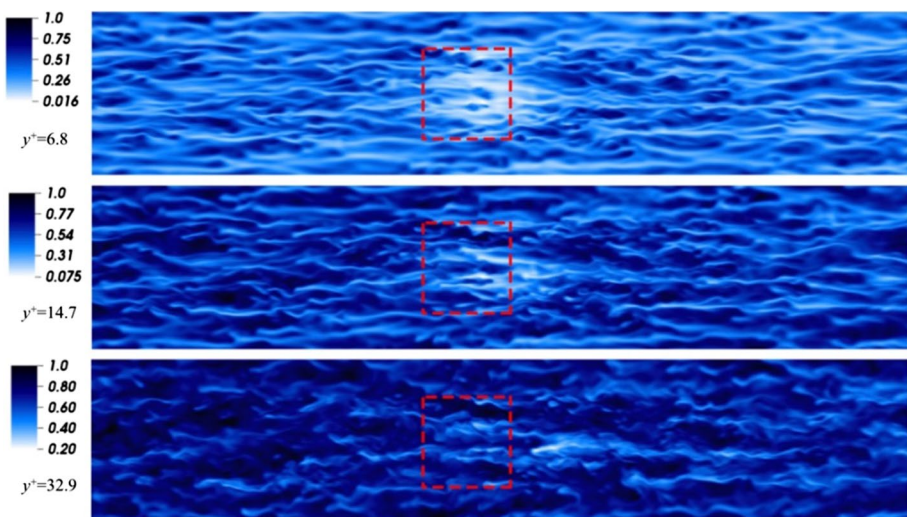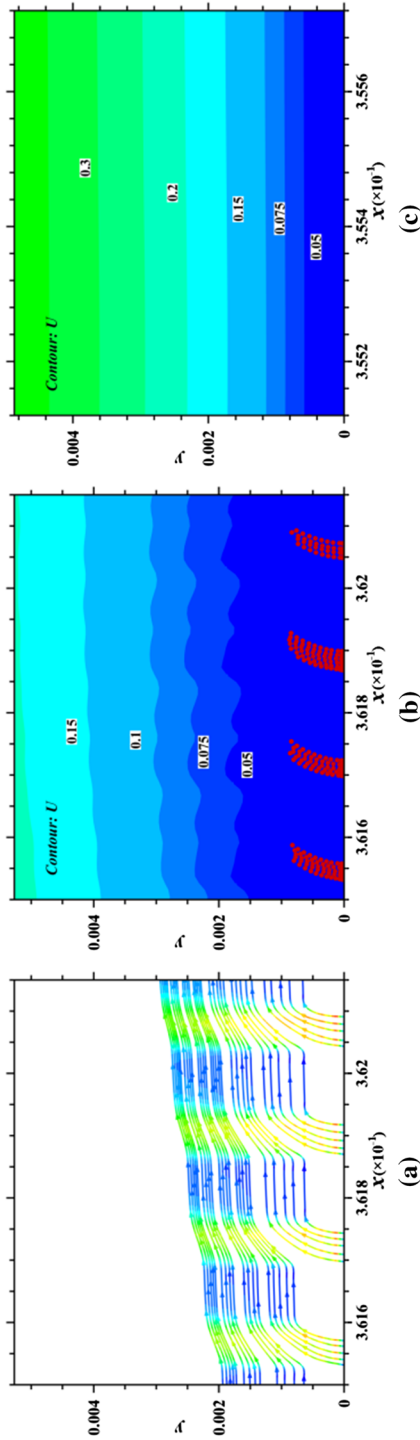

Fig. 9 Instantaneous stream-wise velocity component u contours at $y^+ = 6.8$, 14.7, 32.9

Fig. 10 Time-averaged flow information near the micro-holes (**a** and **b** correspond to micro-blowing case, and **c** denotes the basic flow; note: reduce *x* coordinates by 10 times)

and the velocity gradient is decreased near the wall. Thus, the drag reduction of skin friction can be achieved by micro-blowing control.

Visualization of micro-blowing jet is shown in Fig. 11. The marks 1, 2, 3 and 5, 6, 7 represent locations with and without micro-blowing on the wall, respectively. The distributions of time-averaged stream-wise velocity by Van Driest transformation are presented in Fig. 12. The black circle in Fig. 13a is the calculation result of basic flow, which is consistent with the black solid line obeying the logarithm law in the incompressible turbulent flat-plate boundary layer (Ying et al. 2007; Reichardt 1951). This shows that the compressible effect of the current flat-plate turbulent boundary layer is weak at Ma = 0.7 and the Morkovin hypothesis is valid.
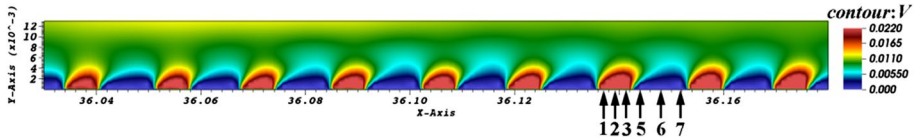
Fig. 11 Normal velocity distribution of blowing

(a) stream-wise velocity U^+-y^+ **(b)** normal velocity V^+-y^+
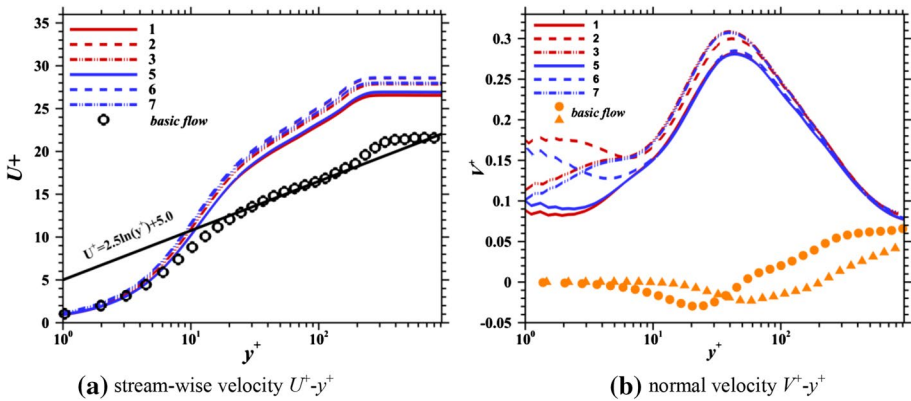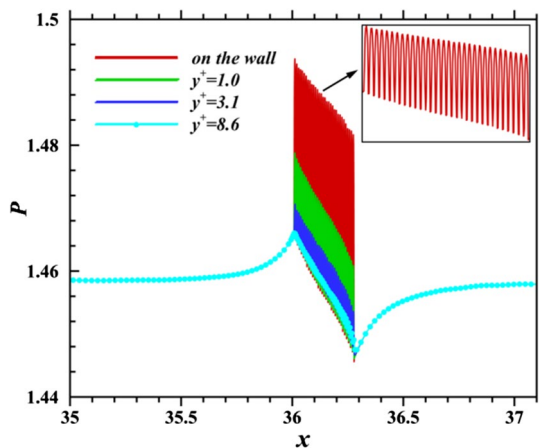
Fig. 12 Van Driest transformed mean velocity profiles in local wall units (circle represents the basic flow)

Fig. 13 Distributions of the mean pressure P near the wall due to micro-blowing

By means of micro-blowing, upward shifts are observed at the logarithmic layer at both of the blowing and the non-blowing locations, which is widely found in other turbulent boundary layer simulations with blowing (Kornilov and Boiko 2014; Park and Choi 1999; Kametani et al. 2015; Kametani and Fukagata 2011). The distribution of stream-wise velocity keeps unchanged at $y^+ > 232$ regarding to $x = 36.142$. Hence, the turbulent friction Reynolds number in present compressible turbulent boundary layer with micro-blowing is considered to be about $Re_\tau = 232$. As for the time-averaged normal velocity, a process of rising firstly and then falling at the logarithmic layer is discovered in the micro-blowing case, and the locations of these peaks are approximately obtained at $y^+ = 38$. Although the peak value is about 4–5 times higher than the basic flow and the scope of normal blowing exceeds $y^+ = 232$, the magnitude of normal velocity is still very small relative to the stream-wise velocity. Thus, the impact of micro-blowing on flow structure is still limited. These similar profiles indicate that the micro-blowing not only affects the flow characteristics in the micro-holes region, but also transmits the similar properties to the no-blowing regions. This is possibly related to the small porosity of 23%. What we can learn from this case is that there is no need to adopt blowing control for all the area, so that we can greatly save the input energy. Kornilov and Boiko (2014) found that the slowly changing of boundary layer characteristics will spread to the whole flat-plate when adopting the non-continuous micro-blowing method, so there is a consistent drag reduction along the chord of the perforated insert including the impermeable sections. With this drag reduction technique, energy efficiency will also be improved.

Figure 13 shows the variations of the time-averaged pressure P in the near-wall region due to micro-blowing. It is seen that the wall pressure changes very quickly near the micro-hole. The adverse pressure gradients occur before and after the micro-hole, and overall favorable pressure gradients occur above the micro-hole. The similar results were also shown in the DNS cases of uniform blowing or suction with a span-wise slot (Park and Choi 1999). But the difference is the up and down pressure fluctuation along the stream-wise direction in the blowing region, which is due to the staggered arrangement of micro-holes. The fluctuation amplitude on the wall is the largest and it descends as moving away from the wall.

3.3 Vorticity Transport

Figure 14 shows a time-averaged spatial distribution of stream-wise vortices in the middle section of $z = L_z/2$. Except for the micro-blowing area, the vorticity after time average is very small in the boundary layer, so the color scale is chosen from -1 to 1. The y^+ is dimensionless by the wall unit chosen at $x = 35.5$ where is far away from the micro-blowing region. It is seen that several small vortices with large positive and negative vorticity, arranged in neat intervals, are distributed in the vicinity of the micro-blowing. This is due to the vertical injection of micro-blowing ($\omega_x = \partial w/\partial y - \partial v/\partial z$). And a pair of positive and negative stream-wise vortices numbered from the upstream inclines upward as it passes by the micro-blowing region, showing that the motions of stream-wise vortices are obviously affected by micro-blowing. This inclination of these coherent structures is also observed in the experimental study of local blowing (Haddad et al. 2007). With the influence of inflow, those jets from the micro-holes develop downstream and converge into two large vortex clusters, which vigorously demonstrates that the influence of blowing develops downstream with a distance (Park and Choi 1999; Liu et al. 2017).
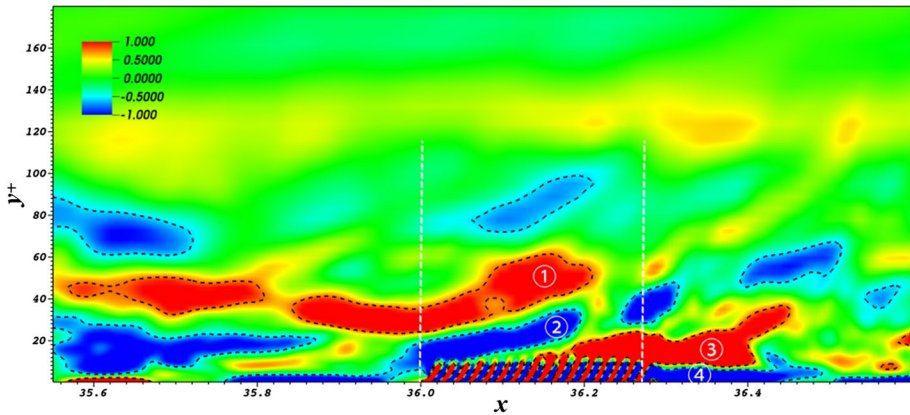
Fig. 14 Time-averaged stream-wise vorticity contour $\overline{\omega}_x$ in the section of $z = L_z/2$

Fig. 15 Curves of mean stream-wise vorticity at different locations
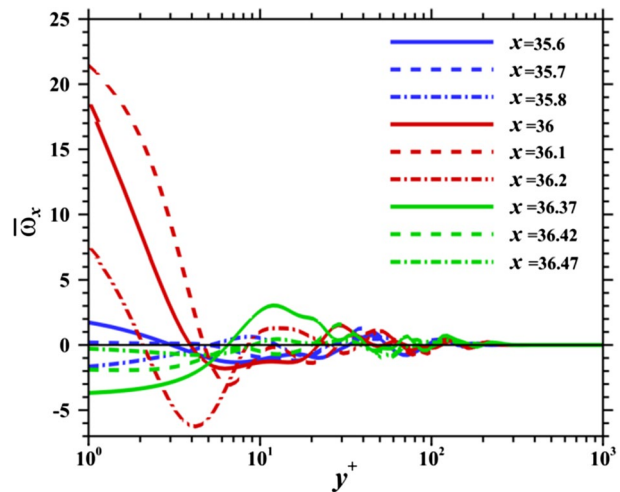
Such complicated vortices structures superimposed in the boundary layer lead to a vorticity field with strong variations. A detailed discussion of quantitative results is shown in Fig. 15. Comparing the two cases before and at the blowing area, the vorticity magnitude at $y^+ < 8$ with micro-blowing (red lines) is significantly larger due to the vertical blowing velocity, while at $y^+ > 10$, they are almost in a same scale and tend to be very small quickly. It indicates that although the vorticity caused by the micro-blowing jet from the solid wall is large enough, it just makes a small contribution to the time-average vorticity at $y^+ > 10$, thus the penetration ability of micro-blowing is still limited. In the downstream area after the micro-blowing control (see $x = 36.37$), the peak values of the positive and negative stream-wise vortices has a small increase ($y^+ \approx 13$) due to the confluence of micro-jets, but the vorticity quickly recovers to the previous state as it moves far away. Actually, we find that the most dominant impact of the micro-blowing on the average vorticity flow field is focused on the viscous sub-layer and downstream

region. Moreover, as the blowing fraction of micro-blowing is weak, the impact in the downstream is also very limited.

In consideration of the vorticity dynamic, the stream-wise vorticity transport equation is written as,

$$\rho \frac{d}{dt}\left(\frac{\omega_x}{\rho}\right) = \omega_x \frac{\partial u}{\partial x} + \left(\omega_y \frac{\partial u}{\partial y} + \omega_z \frac{\partial u}{\partial z}\right) + \frac{1}{\rho^2}\left(\frac{\partial \rho}{\partial y}\frac{\partial p}{\partial z} - \frac{\partial \rho}{\partial z}\frac{\partial p}{\partial y}\right) + \frac{1}{Re}\nabla^2 \omega_x \quad (3\text{-}5)$$

where the first and second terms of the right-hand side in the above equation represent the stretching and tilting, respectively, while the third term for the baroclinicity with the contribution of compressibility, and the last term for the diffusion due to molecular motion. The dynamic equation for the strength of the stream-wise vorticity can be obtained by multiplying both sides of the equation by ω_x,

$$\frac{\rho}{2}\frac{d}{dt}\left(\frac{\omega_x^2}{\rho}\right) = \underbrace{\omega_x^2 \frac{\partial u}{\partial x}}_{\text{S-term}} + \underbrace{\omega_x\left(\omega_y \frac{\partial u}{\partial y} + \omega_z \frac{\partial u}{\partial z}\right)}_{\text{T-term}} + \underbrace{\frac{\omega_x}{\rho^2}\left(\frac{\partial \rho}{\partial y}\frac{\partial p}{\partial z} - \frac{\partial \rho}{\partial z}\frac{\partial p}{\partial y}\right)}_{\text{P-term}} + \underbrace{\frac{\omega_x}{Re}\nabla^2 \omega_x}_{\text{D-term}}$$

$$(3\text{-}6)$$

The change of each term in different stream-wise locations is depicted in Fig. 16, which can help us understand which term mostly affects the evolution of the stream-wise vorticity. Ensemble averages both in time and z space are used to obtain the mean value of each term corresponding to y-axis.

In Fig. 16a, at $y^+ < 10$, the dominant terms for the evolution of the stream-wise vorticity are the tilting and diffusion, while the maximum diffusion is relative larger. Hence, the summary of all term is negative at the viscous sub-layer. At $y^+ > 10$, the stretching has nearly the same magnitude with the tilting and the viscous dissipation is also decreasing, thus a positive summary $d\left(\omega_x^2/\rho\right)/dt$ is obtained, which means that the strength of stream-wise vortices becomes strong as the flow develops. This dynamic evolution of stream-wise vorticity in the no-blowing region matches very well with the studies of Park and Choi (1999) and Brooke and Hanratty (1993).

The variations of each term before and after micro-blowing are presented in Fig. 16b, c, d, e, respectively. In the micro-blowing region (see green lines), the stretching term has a little increase relative to the region before blowing, but it is very close to the black line at the peak. Especially for the tilting term and diffusion term, their peak locations are shifted from $y^+ = 7.5$ to $y^+ = 13$. It indicates that the stream-wise vortices are pushed away from the wall, which is what we saw previously. There are two aspects to consider. The first is the injection direction of micro-jets. It is not absolutely vertical but has some inclined angles (see Fig. 14), due to the effect of the inflow. The second is the accumulation of micro-jets. More mass flow converging at the rear area can lead to a stronger micro-blowing effect downstream, thus the stream-wise vortex is lifted higher. For the area immediately downstream of the blowing region (see red lines), all the stretching, tilting and diffusion terms show a distinct increase, but their peak locations are basically unchanged. This is because the effect of lifting disappears and the stream-wise vortices move close to the near-wall again. Additionally, the momentum of the jet accumulates at this position, which accelerates the transport of vorticity. Thus, the summary of all terms becomes positive. But soon, it returns to its original state in the downstream of $x = 36.47\text{–}38$ (see cyan lines in Fig. 16d). It should be noted that all pressure terms are close to zero at $y^+ > 10$, and the up and down

oscillation at $y^+ < 10$ is related to intern arrangement of micro-blowing (include the oscilla-
tion of D-term), see Fig. 16e.

A temporal evolution of stream-wise fluctuation vorticity ω'_x is presented in Fig. 17. It is
found that the micro-jets in the near-wall region play a very good barrier role in suppress-
ing those fluctuating vortices imposing to the wall surface straightforwardly. Clearly, from
$t = 14$ to $t = 15.5$ before and after the micro-blowing area, the stream-wise vortice cluster
with positive and negative fluctuating values moves forwards and close to the wall, which
creates a high skin friction on the wall (Choi et al. 1993). However, the micro-blowing
jets bring an inhibition of those stream-wise vortices approaching the wall, which cannot
exert force on the wall directly. At this time, the near-wall friction drag is mostly con-
trolled by the local fluctuation motion of micro-blowing air. Thus a drag reduction effect
can be usually obtained, which will be specifically analyzed in the section of friction drag
decomposition.

Figure 18 shows the quantitative comparison of fluctuation vorticity at different stream-
wise locations. In the micro-blowing case, above the micro-holes ($x = 36.1, 36.2$), the y
locations of the maximum and minimum values for the vorticity fluctuations are both
pushed farther away from the wall, thus the near-wall stream-wise vortices are lifted up by
micro-blowing (see Fig. 17). Moreover, its maximum value is a little higher. Similar behav-
ior is observed by Kim and Sung (2006) in DNSs of localized steady blowing in a turbu-
lent boundary layer. In the downstream of micro-blowing ($x = 36.3, 36.5$), the intensity of
the stream-wise vorticity fluctuations becomes obviously stronger with micro-blowing than
that in the basic flat-plate flow, but its position of local maximum gradually recovers to
the same as the basic one, which can also be seen from the averaged stream-wise vorticity
evolution in Fig. 14.

### 3.4 Turbulent Velocity Fluctuation

The root-mean-square (RMS) of velocity fluctuations scaled by local wall units in stream-
wise, wall-normal and span-wise directions are plotted in Fig. 19. Above the micro-holes,
the RMS amplitudes are increased by micro-blowing, and the Reynolds normal stress dom-
inates in the stream-wise direction. The positions of the maximum values on u' remain
basically the same at $y^+ \approx 15$ due to the local non-dimensionalization (Kametani et al.
2015). Previously mentioned the lifted mechanism, the interaction between the stream-wise
vorticity and near-wall small scales becomes weaker, but the micro-blowing injects more
energy into the lift vortices, thus the intensity of stream-wise vortices becomes stronger
and its increasing in downstream is mostly due to the accumulation of jets (see Fig. 14).
Hence, the effect of micro-jets on the stream-wise vortices results in the enhancement of
turbulence intensity, as also apparent for the mean fluctuation vorticity profiles correspond-
ingly. Similarly, the Reynolds shear stress (RSS) is presented in Fig. 20. The curves show
that the maximum value of $<u'v'>$ is gradually increased to above 1.2 in the micro-blow-
ing case, which is about 1.5 times of that in the basic flow. Along the downstream of the
micro-blowing region, the magnitude of RSS increases slightly. It can be concluded that
the intensity of the outer-layer structures is effectively enhanced by the weak amount of
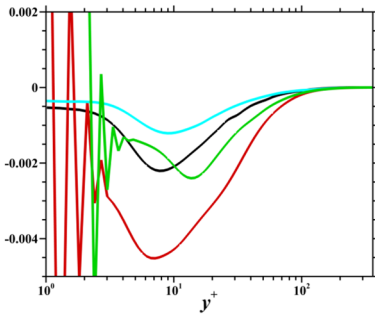micro-blowing.
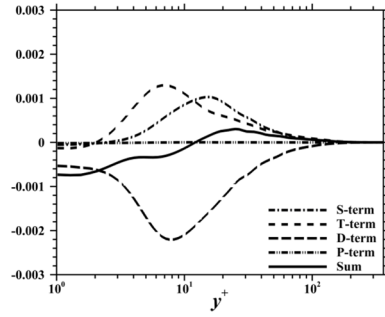
(a) x=34.8~35.8 before the micro-blowing region
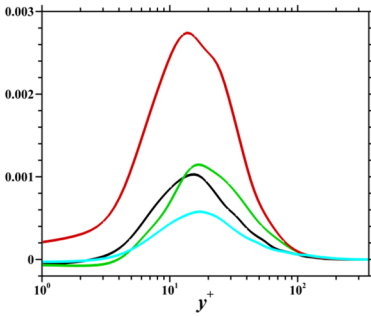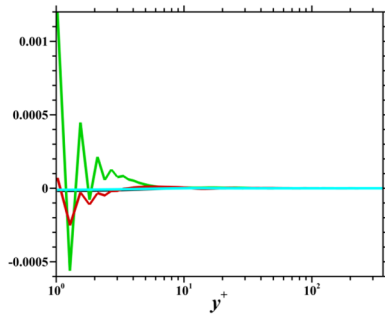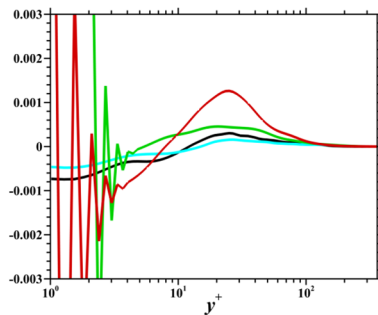

(b) S-term
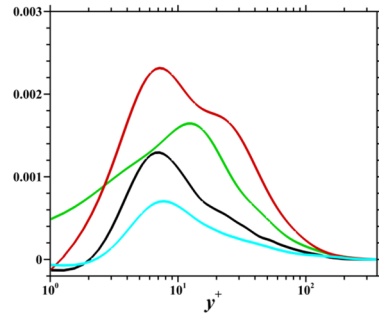
(c) T-term

(d) D-term

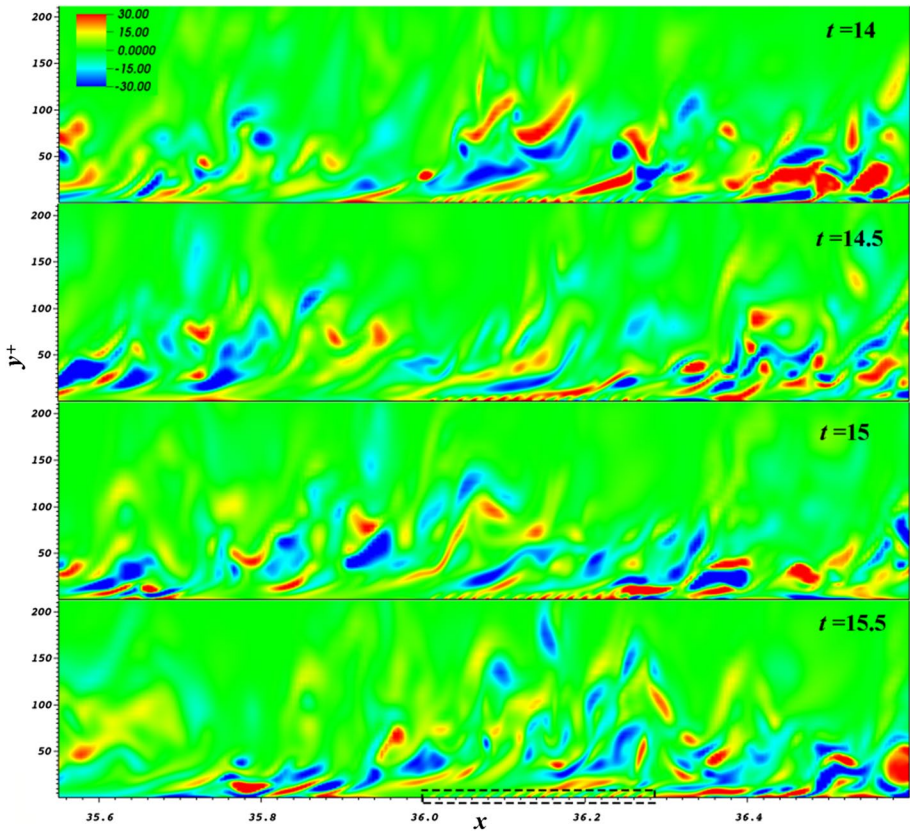
(e) P-term

(f) Sum-term

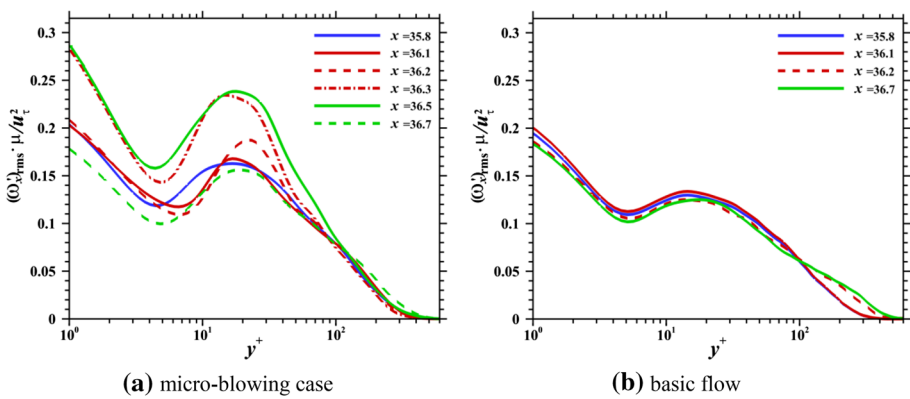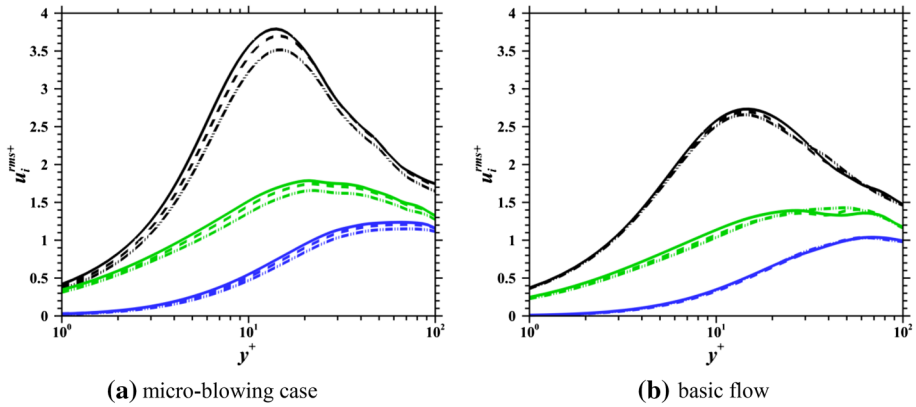**Fig. 17** Evolution contours of stream-wise vorticity fluctuation ω_x' in the x direction

(a) micro-blowing case   **(b)** basic flow

**Fig. 18** Curves of stream-wise vorticity fluctuation at different locations

(a) micro-blowing case   **(b)** basic flow

Fig. 19 Curves of the root-mean-square of velocity fluctuation (black: *u'*; blue: *v'*; green: *w'*; DashDD: 36.1; dashed: 36.15; solid: x = 36.2)

(a) micro-blowing case   **(b)** basic flow
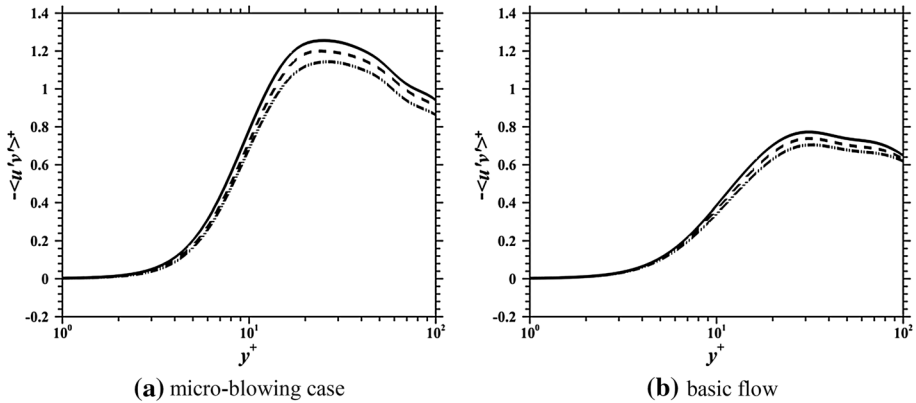
Fig. 20 Curves of Reynolds shear stress *u'v'*

Figure 21a gives the visualizations of the stream-wise velocity fluctuations at $y^+ = 12.8$ in both micro-blowing and basic cases. Interestingly, a sunken black hole can be clearly seen in the micro-blowing control region where it is identified by the green dashed lines. This visual difference is due to the fact that this region is filled with more negative fluctuations, compared with the surrounding area. In this way, no matter in the stream-wise or span-wise direction, the features of fluctuating streak are discontinuous. It is also found that the area of black hole is beyond the control area of micro-blowing, indicating a downstream impact.

By the method of Huang-Hilbert Empirical Mode Decomposition (EMD), the fluctuating information near the micro blowing region is decomposed into four modes. At present, we choose the first mode to represent the small scales and the last three for the large scales (Agostini and Leschziner 2014). As a useful decomposition algorithm, the EMD can acquire some physically meaningful modal information derived from the original signal. As the friction Reynolds number in the current simulation is too low with $Re_\tau \approx 232$, the scale separation between the inner and outer peaks is not clear. After repeated tests, we
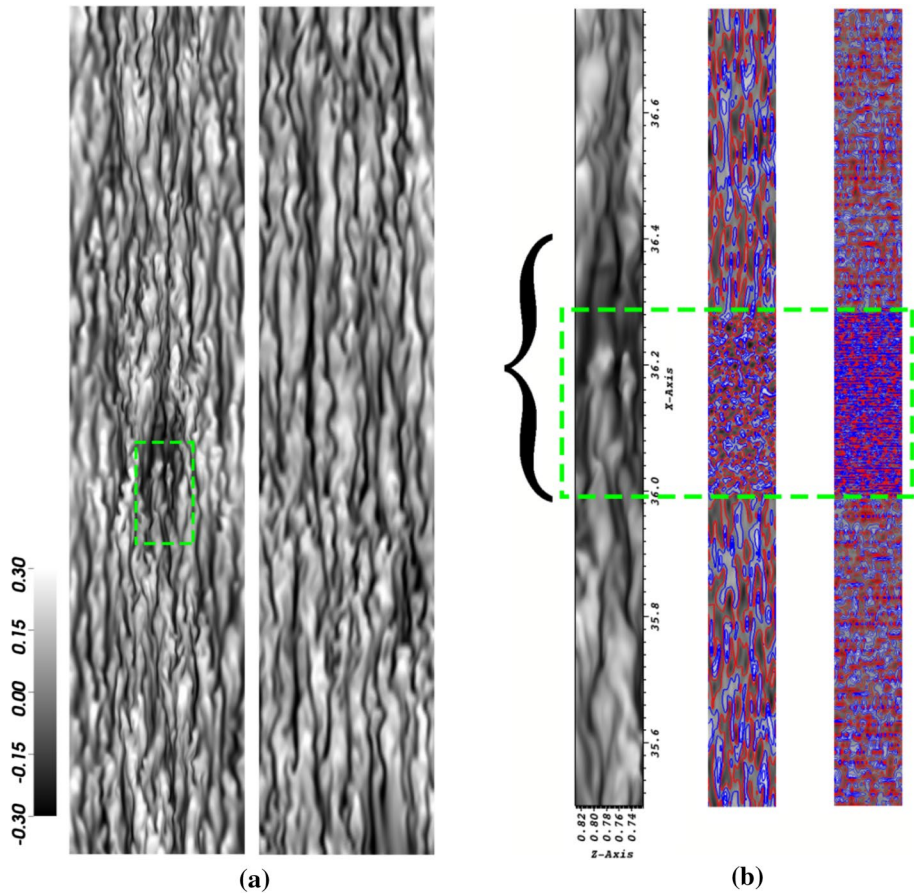
Fig. 21 Contours of stream-wise velocity fluctuations *u'* at $y^+ = 12.8$. (21a: left, micro-blowing case; right, basic flow; 21b: left, complete signal; middle, 2nd + 3rd + 4th mode; right, 1st mode; red/blue identify positive/negative fluctuations with $(-0.3, 0.3)$)

adopt 4 modes for the low Reynolds number case, and this is because the energy proportion of the 4th intrinsic mode is very small after 3 decompositions. In Fig. 21b, no matter large scales or small scales, their structures in the micro-blowing region are relatively broken, compared with that in the upstream and downstream. Due to the arrangement of blowing holes both in the stream-wise *x* and span-wise *z* directions, the stream-wise extended scales seem to be isotropic and are mixed together (Chung et al. 2002; Keirsbulck et al. 2006). Especially, those small scales with positive/negative fluctuations tend to be more compact, indicating that the number of small-scale structures is increasing. In the analyses of power spectra by Kametani et al. (2015), it is also found that blowing increases the small and short wavelength component and spreads the range of wavelength and wall-distance of the spectra. It can be concluded that the micro-blowing has an impingement on large and small scales and brings about more tiny turbulent structures. The visualization of 3D vortex structures near the wall is shown in Fig. 22. The vertical weak jets ejected from the micro-holes form a series of spherical vortices near the wall, and their magnitude of Q_2
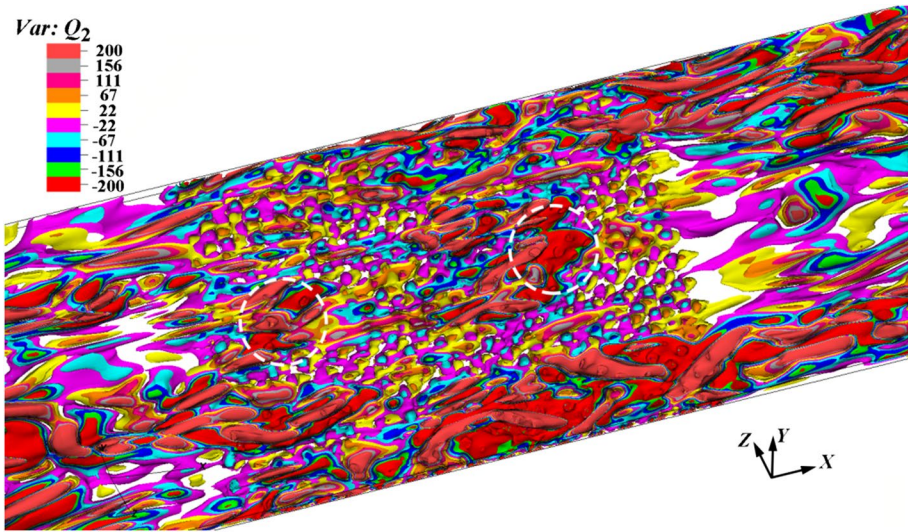
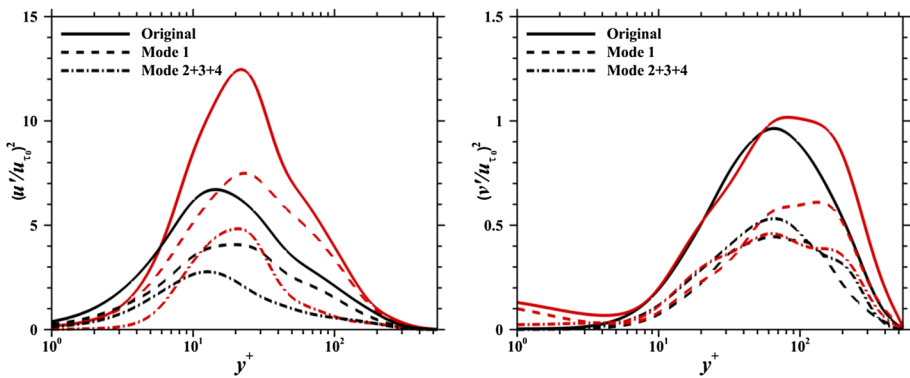**Fig. 22** Visualization of 3D vortex structures near the wall

Fig. 23 Turbulent kinetic energy of stream-wise and normal fluctuation at different modes (red: micro-blowing case; black: basic flow)

ranges from -22 to 22. A force seems to be imposed on the near-wall stream-wise vortices, thus it generates several concave marks on the surface of the near-wall vortices (see white dashed circle), which are the traces of vortex breaking.

Quantitatively, comparisons of the turbulent kinetic energy for large/small scales in the micro-blowing region are presented in Fig. 23. The average in space $36 \leq x \leq 36.2$ is adopted to obtain the mean values. The normalized fluctuating velocity $u_{\tau 0}$ is chosen at $x = 35.5$ in the basic flat-plate flow. For the original fluctuating signals, regardless of u' or v', the turbulent intensities go up with micro-blowing and their peaks slightly move outward, which has been discussed in RMS profiles and vorticity transport. It is found that the small scales (1st mode) occupy more turbulence energy than large scales.

And by micro-blowing, the increment of stream-wise turbulent kinetic energy for small scales is nearly eight times, which also exceeds the large scales. Especially for the normal turbulent kinetic energy, it is mainly manifested in small-scale changes, however, for the large scales it has a slightly drop. It can be concluded that the micro-blowing injects more energy into small scale so more petty turbulence can be found near the wall, just like the qualitative analysis before.

3.5 Decomposition of Skin Friction Drag

A useful mathematical model (referred to as FIK identity) is proposed by Fukagata et al. (2002) to reveal the relationship between the Reynolds shear stress and the skin friction coefficient in the incompressible wall-bounded turbulent flows. For the spatially developing flat-plate turbulent boundary layer, the local skin friction coefficient c_f is decomposed into five contributions: the contributions from boundary layer thickness c^δ, Reynolds shear stress c^T, mean convection c^C, spatial development c^D and pressure gradient c^P. The aim is to find out the dynamical effects of different contributions to the skin friction drag. Noted that the compressibility effect in current flat-plate turbulent boundary layer is weak due to the magnitude of local turbulent Mach number M_t approximately in the range of 0.1 where $M_t = \sqrt{\overline{u'^2} + \overline{v'^2} + \overline{w'^2}} \Big/ \overline{a}$ (a is the local sound speed), thus we still adopt the incompressible FIK identity (Hwang 2004; Karlsson and Johansson 1986).

$$
c_f(x) = \underbrace{\frac{4}{Re_\delta}\left[1 - \delta_d\right]}_{c^\delta} + \underbrace{2\int_0^1 2(1-y)\left(-\overline{u'v'}\right)dy}_{c^T} + \underbrace{2\int_0^1 2(1-y)(-UV)dy}_{c^C}
$$
$$
\underbrace{-2\int_0^1 (1-y)^2\left(\frac{\partial UU}{\partial x} + \frac{\partial \overline{u'u'}}{\partial x} - \frac{1}{Re}\frac{\partial^2 U}{\partial x \partial x}\right)dy}_{c^D} - \underbrace{2\int_0^1 (1-y)^2\frac{\partial P}{\partial x}dy}_{c^P}
$$

$$(3\text{-}7)$$

All terms are normalized by the free inflow U_∞ and the 99% boundary layer thickness δ_{99}. Figure 24 shows the decomposition of FIK identity in the micro-blowing case.
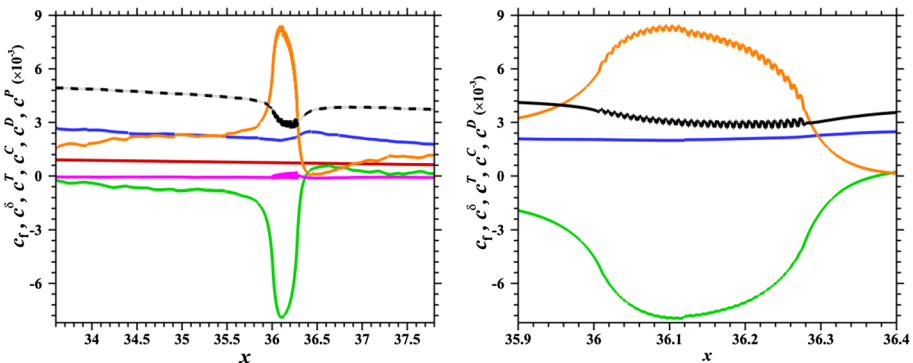
Fig. 24 Decomposition of skin friction drag (right: local enlarged view) (red: c^δ; blue: c^T; green: c^C; orange: c^D; magenta: c^P; black solid line: sum; Dashed line: c_f calculated by velocity gradient on the wall)

In the spatially developing boundary layers, both terms of the Reynolds shear stress (c^T) and the spatial development (c^D) increase the skin friction drag ($c^T > 0$, $c^D > 0$), while the contribution from the mean convection (c^C) reduces it ($c^C < 0$). Moreover, the contribution of the boundary layer thickness c^δ occupies a very small part compared with the others. A small fluctuation of c^P occurs in the micro-blowing region due to the pressure gradient before and after staggered holes (see in Fig. 13). However, the pressure before and after the blowing location keeps basically the same. Thus, in a small blowing fraction, the drag contribution from the pressure gradients is tiny, which is similar to the results of Kametani et al. (2015) In the micro-blowing region, the Reynolds shear stress term c^T increases a little, but the negative mean convection term has a sharp decline, which exceeds the increment of positive spatial development term. Consequently, a global drag reduction on the micro-blowing wall can be obtained. These trends found here are similar to the ones in the spatially developing turbulent boundary layer with uniform blowing/suction by Kametani and Fukagata (2011). Above analyses indicate that the mean wall-normal convection term c^C plays a decisive role in the contribution of the drag reduction.

In the right view of Fig. 24, a small fluctuation can be found in both spatial development term c^D and the sum of skin friction coefficient c_f, which is mainly dominated by the non-continuous arrangement of micro-holes, see Fig. 25. A series of concentric ring structures occur in the near-wall region due to the micro-blowing, and these flow characteristics with different attribute values are distributed at intervals along the stream-wise direction. That is the source of the pulse. In terms of intensity, the magnitude of the term $\partial UU/\partial x$ is significantly greater than the other two, which indicates that the gradient of stream-wise kinetic energy dominates the enhancing level of skin friction drag. The large blowing fraction may usually bring about the strong gradient. This is why the blowing intensity cannot be too high.

For the contribution c^C from the normal-wall mean convection, a large hemispherical region with negative values is formed above the micro-blowing region, although the
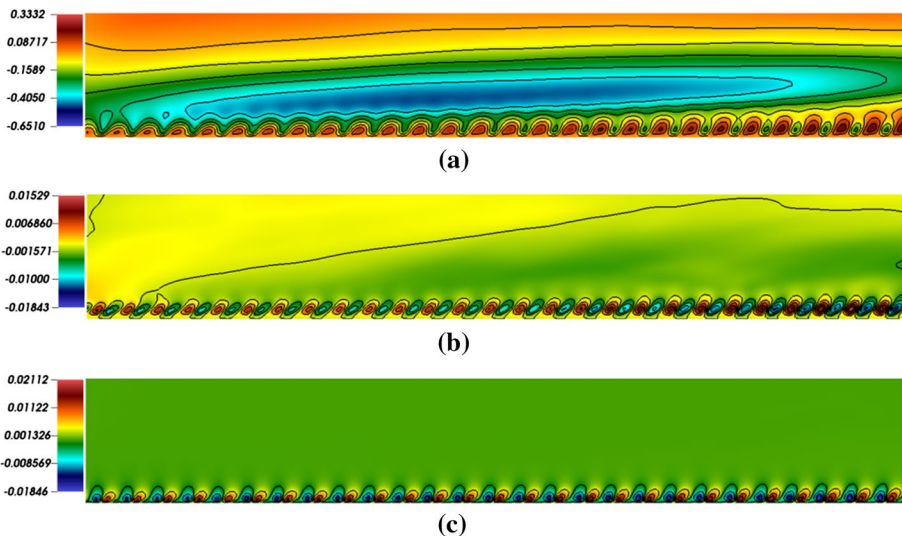

Fig. 25 Contours of three terms in the middle x–y section (a: $\frac{\partial UU}{\partial x}$; b: $\frac{\overline{\partial u'u'}}{\partial x}$; c: $\frac{1}{Re}\frac{\partial^2 U}{\partial x \partial x}$)
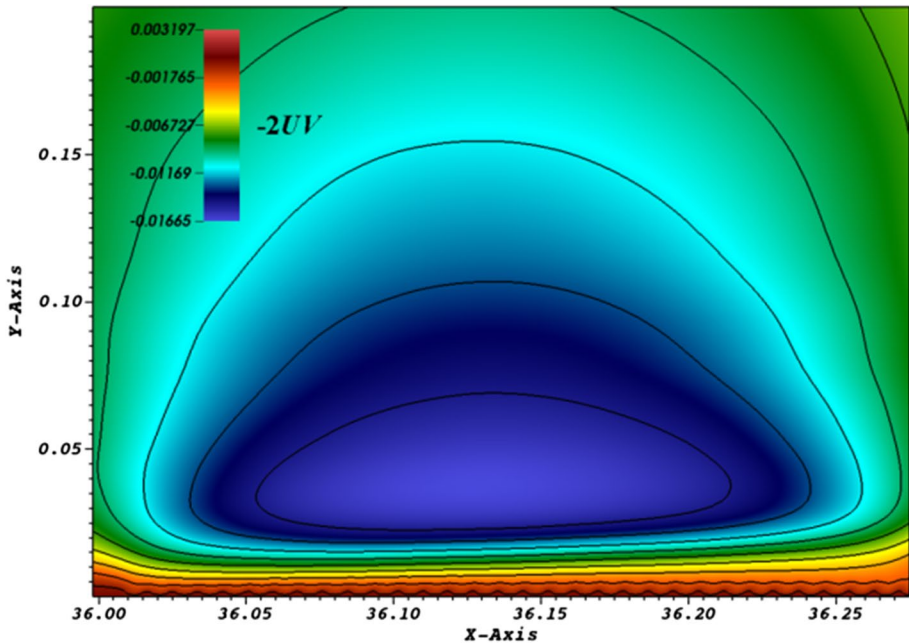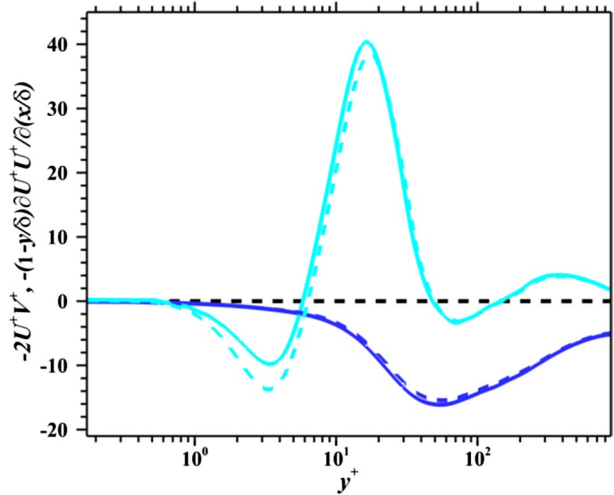
Fig. 26 Contour of $-2UV$ in the term c^C in the middle x–y section

Fig. 27 Curves of different terms in the contributions of c^C (cyan) and c^D (blue) (solid line: $x=36.15$; dashed line: $x=36.2$)

near-wall area is filled with a few small positive values, see Fig. 26. Exactly, the total integral in the turbulent boundary layer leads to a critical decrease to make an important contribution to the drag reduction. The comparison of two contributions c^C and c^D is shown in Fig. 27, and we omit a few small amounts in the term of c^D. It is clearly that the peak magnitude in c^D is relatively larger but its impact area in the normal is smaller, compared with the c^C. Apparently, we can find that the impact area of c^C ranges from the near-wall

sub-layer to the outer layer beyond $y^+ = 100$, and the peak point is further away from the wall. This fact indicates that the formation of the larger normal convection area by $-2U^+V^+$ above the micro-blowing plays a dominant role in the skin friction drag reduction from the decomposition of drag.

4 Conclusions

In this paper, the DNS of a spatially developing boundary layer on a flat plate with localized micro-blowing is applied to study the effects of micro-blowing. The numerical results show that there is a low-speed "turbulent spot" near the micro-holes region. This low-speed "turbulent spot" induces an area with lower velocity gradient near the wall, leading to effective drag reduction. In the micro-blowing region, the dynamics of vorticity transport shows that the peak of tilting term is shifted from $y^+ = 7.5$ to $y^+ = 13$, while its peak value is increased. The micro-blowing uplifts the stream-wise vortices and makes it more tilting. Due to the accumulation of mass flux of micro-jets, in the near downstream region of the micro-blowing, all terms of vorticity transport equation and vorticity fluctuations have an obvious increase in intensity, but their peaks return to its original location. The micro-blowing plays a good barrier in suppressing the ejection/sweep events imposed to the surface of the wall, which is also due to the influence of the uplift mechanism. For 3D vortex visualization, several concave marks are observed on the surface of the near-wall vortices. The impingement exerted by micro-jets on near-wall turbulent structures leads to more broken small scales. Moreover, the distribution of turbulent scales in both stream-wise and span-wise directions tends to be isotropic in the micro-blowing region.

The numerical results prove that the micro-blowing flow control is effective on drag reduction. The local drag is reduced by up to 40%. The area of drag reduction not only covers the entire micro-blowing region, but also extends to a short distance downstream. The analysis of FIK identity reveals that the spatial development terms of stream-wise kinetic energy c^D and mean wall-normal convection term c^C play a decisively positive and negative role, respectively, in the contribution of the skin friction drag in the spatially developing flat-plate boundary layer. Although the peak value of c^C is relatively smaller and its location is further away from the wall, the impact area of the mean convection term is much larger ranging from the near-wall sub-layer to the outer layer, therefore, its integral forms a drag reduction.

Compliance with Ethical Standards

Conflict of interest The authors declare that they have no conflict of interest.

References

Abderrahaman-Elena, N., García-Mayoral, R.: Analysis of anisotropically permeable surfaces for turbulent drag reduction. Phys. Rev. Fluids **2**(11), 114609 (2017). https://doi.org/10.1103/PhysRevFluids.2.114609

Agostini, L., Leschziner, M.A.: On the influence of outer large-scale structures on near-wall turbulence in channel flow. Phys. Fluids **26**(7), 075107 (2014). https://doi.org/10.1063/1.4890745

Araya, G., Leonardi, S., Castillo, L.: Steady and time-periodic blowing/suction perturbations in a turbulent channel flow. Physica D **240**(1), 59–77 (2011). https://doi.org/10.1016/j.physd.2010.08.006

Brooke, J.W., Hanratty, T.J.: Origin of turbulence-producing eddies in a channel flow. Phys. Fluids A **5**, 1011–1022 (1993). https://doi.org/10.1063/1.858666

Choi, H., Moin, P., Kim, J.: Direct numerical simulation of turbulent flow over riblets. J. Fluid Mech. **255**, 503–539 (1993). https://doi.org/10.1017/S0022112093002575

Chung, Y.M., Sung, H.J.: Initial relaxation of spatially evolving turbulent channel flow with blowing and suction. AIAA J. **39**(11), 2091–2099 (2001). https://doi.org/10.2514/2.1232

Chung, Y.M., Sung, H.J., Krogstad, A.P.: Modulation of near-wall turbulence structure with wall blowing and suction. AIAA J. **40**(8), 1529–1535 (2002). https://doi.org/10.2514/2.1849

Du, Y., Karniadakis, G.E.: Suppressing wall turbulence by means of a transverse traveling wave. Science **288**(5469), 1230–1234 (2000). https://doi.org/10.1126/science.288.5469.1230

Fu, D., Ma, Y., Li, X., et al.: Direct Numerical Simulation of Compressible Turbulence. Science Press, Beijing (2010)

Fukagata, K., Iwamoto, K., Kasagi, N.: Contribution of Reynolds stress distribution to the skin friction in wall-bounded flows. Phys. Fluids **14**(11), L73–L76 (2002). https://doi.org/10.1063/1.1516779

Haddad, M., Labraga, L., Keirsbulck, L.: Effects of blowing through a porous strip in a turbulent channel flow. Exp. Therm. Fluid **31**(8), 1021–1032 (2007). https://doi.org/10.1016/j.expthermflusci.2006.10.007

Hwang, D.: Review of research into the concept of the microblowing technique for turbulent skin friction reduction. Prog. Aerosp. **40**(8), 559–575 (2004). https://doi.org/10.1016/j.paerosci.2005.01.002

Hwang, D.: A proof of concept experiment for reducing skin friction by using a micro-blowing technique. In: 35th Aerospace Sciences Meeting and Exhibit, p. 546 (1997). https://doi.org/10.2514/6.1997-546

Kametani, Y., Fukagata, K.: Direct numerical simulation of spatially developing turbulent boundary layers with uniform blowing or suction. J. Fluid Mech. **681**, 154–172 (2011). https://doi.org/10.1017/jfm.2011.219

Kametani, Y., Fukagata, K., Orlu, R., Schlatter, P.: Drag reduction in spatially developing turbulent boundary layers by spatially intermittent blowing at constant mass-flux. J. Turbul. **17**, 913 (2016). https://doi.org/10.1080/14685248.2016.1192285

Kametani, Y., Fukagata, K., Örlü, R., Schlatter, P.: Effect of uniform blowing/suction in a turbulent boundary layer at moderate Reynolds number. Int. J. Heat Fluid Flow **55**, 132–142 (2015). https://doi.org/10.1016/j.ijheatfluidflow.2015.05.019

Karlsson, R.I., Johansson, T.G.: LDV measurements of higher order moments of velocity fluctuations in a turbulent boundary layer. In: 3rd International Symposium on Applications of Laser Anemometry to Fluid Mechanics (1986)

Keirsbulck, L., Labraga, L., Haddad, M.: Influence of blowing on the anisotropy of the Reynolds stress tensor in a turbulent channel flow. Exp. Fluid **40**(4), 654 (2006). https://doi.org/10.1007/s00348-005-0105-6

Kim, K., Sung, H.J.: Effects of unsteady blowing through a spanwise slot on a turbulent boundary layer. J. Fluid Mec. **557**, 423–450 (2006). https://doi.org/10.1017/S0022112006009906

Komminaho, J., Skote, M.: Reynolds stress budgets in Couette and boundary layer flows. Flow Turbul. Combust. **68**, 167–192 (2002). https://doi.org/10.1023/A:1020404706293

Kornilov, V.I.: Current state and prospects of researches on the control of turbulent boundary layer by air blowing. Prog. Aerosp. **76**, 1–23 (2015). https://doi.org/10.1016/j.paerosci.2015.05.001

Kornilov, V.I., Boiko, A.V.: Efficiency of air microblowing through microperforated wall for flat plate drag reduction. AIAA J. **50**(3), 724–732 (2012). https://doi.org/10.2514/1.J051426

Kornilov, V.I., Boiko, A.V.: Flat-plate drag reduction with streamwise noncontinuous microblowing. AIAA J. **52**(1), 93–103 (2014). https://doi.org/10.2514/1.J052477

Krogstad, P.Å., Kourakine, A.: Some effects of localized injection on the turbulence structure in a boundary layer. Phys. Fluids **12**(11), 2990–2999 (2000). https://doi.org/10.1063/1.1314338

Lardeau, S., Leschziner, M.A.: The streamwise drag-reduction response of a boundary layer subjected to a sudden imposition of transverse oscillatory wall motion. Phys. Fluids **25**(7), 075109 (2013). https://doi.org/10.1063/1.4816290

Liu, C., Araya, G., Leonardi, S.: The role of vorticity in the turbulent/thermal transport of a channel flow with local blowing. Comput. Fluids **158**, 133–149 (2017). https://doi.org/10.1016/j.compfluid.2016.12.020

Park, J., Choi, H.: Effects of uniform blowing or suction from a spanwise slot on a turbulent boundary layer flow. Phys. Fluids **11**(10), 3095–3105 (1999). https://doi.org/10.1063/1.870167

Pirozzoli, S., Grasso, F., Gatski, T.B.: Direct numerical simulation and analysis of a spatially evolving supersonic turbulent boundary layer at M= 2.25. Phys. Fluids **16**(3), 530–545 (2004). https://doi.org/10.1063/1.1637604

Poinsot, T.J.A., Lelef, S.K.: Boundary conditions for direct simulations of compressible viscous flows. J. Comput. Phys. **101**(1), 104–129 (1992). https://doi.org/10.1016/0021-9991(92)90046-2

Reichardt, H.: Complete representation of the turbulent velocity distribution in smooth pipe. Z. Angew Math. **31**, 208–219 (1951)

Schlatter, P., Orlu, R., Li, Q., Brethouwer, G., Fransson, J.H., Johansson, A.V., Alfredsson, P.H., Henningson, D.S.: Turbulent boundary layers up to Reθ=2500 studied through simulation and experiment. Phys. Fluids **21**, 051702 (2009). https://doi.org/10.1063/1.3139294

Schlatter, P., Örlü, R.: Assessment of direct numerical simulation data of turbulent boundary layers. J. Fluid Mech. **659**, 116–126 (2010). https://doi.org/10.1017/S0022112010003113

Schlatter, P., Örlü, R.: Turbulent boundary layers at moderate Reynolds numbers: inflow length and tripping effects. J. Fluid Mech. **710**, 5–34 (2012). https://doi.org/10.1017/jfm.2012.324

Smits, A.J., Matheson, N., Joubert, P.N.: Low-Reynolds-number turbulent boundary layers in zero and favourable pressure gradients. J. Ship Res. **27**, 147–157 (1983). https://doi.org/10.1016/0022-1694(83)90034-3

Stroh, A., Frohnapfel, B., Schlatter, P., Hasegawa, Y.: A comparison of opposition control in turbulent boundary layer and turbulent channel flow. Phys. Fluids **27**(7), 075101 (2015). https://doi.org/10.1063/1.4923234

Sumitani, Y., Kasagi, N.: Direct numerical simulation of turbulent transport with uniform wall injection and suction. AIAA J. **33**(7), 1220–1228 (1995). https://doi.org/10.2514/3.12363

Tillman, T.G., Hwang, D.P.: Drag reduction on a large-scale nacelle using a microblowing technique. In: 37th AIAA Aerospace Sciences Meeting and Exhibit, Reno, NV, AIAA Paper 1999–0130. https://doi.org/https://doi.org/10.2514/6.1999-130 (1999)

Wu, X., Moin, P.: Transitional and turbulent boundary layer with heat transfer. Phys. Fluids. **22**, 085105 (2010). https://doi.org/10.1063/1.3475816

Ying, Z., Xin-Liang, L., De-Xun, F., Yan-Wen, M.: Coherent structures in transition of a flat-plate boundary layer at Ma= 0.7. Chin. Phys. Lett. **24**(1), 147 (2007). https://doi.org/10.1088/0256-307X/24/1/040